Electronic version of an article published as
Journal of Medical Robotics Research, Vol. 9, No. 03n04 (2024) 2440005
© World Scientific Publishing Company
doi: 10.1142/S2424905X24400051

Mitigating Singularities in Control of Magnetic Capsule Endoscopes Using a Novel Nested Electromagnetic Coil System

Xinhao Chen[a], Anuruddha Bhattacharjee[a], Lamar O. Mair[b], Suraj Raval[c], Pranav Addepalli[d], Onder Erin[a], Adrian Bell[d], Yancy Diaz-Mercado[c], Axel Krieger[a,d]

[a]*Laboratory for Computational Sensing and Robotics, Johns Hopkins University, Baltimore, MD 21218, USA*
E-mail: xchen254@jhu.edu

[b]*Division of Magnetic Manipulation and Particle Research, Weinberg Medical Physics, MD 20852, USA*

[c]*Department of Mechanical Engineering, University of Maryland, College Park, MD 20742, USA*

[d]*Department of Mechanical Engineering, Johns Hopkins University, Baltimore, MD 21218, USA*

Magnetic actuation systems that utilize external electromagnetic coils present a promising approach for controlling untethered small-scale robots, notably in medical applications. However, these systems frequently experience control singularities that significantly affect the robots' stability in specific areas of the workspace. In order to effectively mitigate these control singularities, this paper introduces a closed-loop control method using a novel nested electromagnetic coil system, leveraging finite element analysis-based magnetic field data and singularity solvers. The electromagnetic system is a 12-coil system with variable outer radius individually addressable coil stacks (VORIACS). Here, we experimentally evaluate the method for closed-loop trajectory tracking of a soft magnetic capsule endoscope (PillCam™) inside the VORIACS system at different magnetic field orientations. The results demonstrate that the VORIACS system with a singularity solver reduces root mean square position tracking errors of the PillCam™ by 46% to 50% and orientation tracking error by 41% to 42% compared to a standard 4-coil system. We further manipulate the PillCam™ for tracking a medical application-inspired complex trajectory, showcasing the system's potential in precise control of magnetic devices for medical use.

Keywords: Medical robotics; capsule endoscopy; magnetic control.

1. Introduction

Magnetic actuation offers significant potential for manipulating miniature medical robots inside the human body.[1,2] Magnetic fields generated by electromagnetic coil systems[3] can safely penetrate most biological tissues and organs for manipulation of magnetic tools via the application of forces and torques. Wirelessly controlled miniature magnetic robots are capable of performing ultra-minimally invasive medical procedures, such as capsule endoscopy,[4] biopsy,[5] suturing,[6–8] and targeted drug delivery.[9] These magnetic tools may benefit both surgeons and patients by reducing surgical complications and patient discomfort.

Capsule endoscopes are noninvasive medical devices that can be swallowed to capture images of the gastrointestinal (GI) tract using onboard miniature cameras, allowing physicians to assess a patient's delicate internal GI surfaces and tissues with minimal discomfort.[10] Due to its noninvasive nature, capsule endoscopy has found extensive application in the assessment and identification of conditions such as Crohn's disease, small bowel tumors, and polyp syndrome.[11] Traditional GI capsule endoscopes, such as the PillCam™ COLON 2 System from Medtronic, depend on passive locomotion (i.e., GI peristalsis), and so lack the localization and controllability required for precise maneuvering near a specific target. External magnetic control can enhance the locomotion capability of these devices, extending functionality. Moreover, magnetic guidance can allow precise control of the position and orientation of the capsule robot, which may help avoid undesired pressure in the intestine wall and may mitigate the risk of GI injury.[12] However, the safe and precise manipulation of a magnetic capsule robot depends on an accurate estimate of externally applied magnetic forces and torques. Magnetic dipole models are reliable for estimating forces and torque far from the magnetic source but may yield large errors near the field source.[13] Finite element analysis (FEA) based modeling of the magnetic field enhances estimation accuracy of the

near-source magnetic field.[14,15]

Electromagnetic systems (EMS) with more coils than their kinematic degrees of freedom may exhibit unforeseen singularities that occur exclusively under particular object orientations.[16] Such orientation-dependent singularities, of EMS, arising from an ill-conditioned matrix in the inverse magnetic calculation, may affect the spatial controllability of magnetic agents. Implementing the Tikhonov regularization method[17] in addition to a model reference adaptive controller[18] or a traditional PID controller[19] may help address this issue. While these approaches have been effective in solving singularities for selective trajectories, they either ignored error-dominated workspace regions or had large tracking errors. Therefore, a new control method is necessary to solve the orientation-dependent singularity of EMS and ensure high-precision control of magnetic agents over the entire workspace.

This paper presents a closed-loop control method that integrates FEA-based magnetic field estimation of electromagnets with singularity solvers and a PID controller for accurate position and orientation control of magnetic agents in any region inside an EMS. The primary contributions of this paper are 1) FEA-based accurate magnetic field estimation of a custom 12-coil electromagnetic system (VORIACS),[20] 2) A novel controller that combines singularity solver and optimal current control for mitigating the singularities in VORIACS, 3) A closed-loop control method that utilizes FEA-based magnetic field data, singularity solver, and a PID controller for vision-based position and orientation control of a magnetic PillCam™ capsule endoscope,4) Experimental evaluation of the closed-loop control method with varied numbers of coils and different singularity solvers for trajectory tracking of a PillCam™ at specific magnetic field orientations, 5) An experimental demonstration of the closed-loop control method for magnetic guidance of a PillCam™ inspired by a medical application.

2. Methods

2.1. *Electromagnet Array and Experimental Setup*

The electromagnetic manipulator used in this study is a custom-built 12-coil system with variable outer radius individually addressable coil stacks (VORIACS),[20] which is capable of generating stronger magnetic gradients (3768 mT/m at the center of a 100×100 mm^2 workspace) and is suitable for wireless manipulation of small-scale magnetic objects. Six motor drivers (Roboclaw, 2x60AHV), operated in two-channel mode and powered by six power supplies (SL Power, TF3000A60K), are used to control all twelve coils individually. Each power supply is rated to supply 60 V at 50 A. A custom MATLAB program on a dedicated CPU (i7-13700KF) was utilized to interface the motor divers via a microcontroller (Teensy). The microcontroller utilizes pulse width modulation (PWM) signals to initiate the motor drivers, subsequently powering the coils.

Our experimental setup consists of the electromagnetic system (VORIACS), 3D-printed workspaces, a magnetic agent (PillCam™), and a digital camera (FLIR BFS-U3-13Y3) mounted to a revolving arm over the workspace. Two 3D-printed workspaces with flat and wavy boundary walls (to mimic walls of the GI tract) were used to conduct experiments inside the VORIACS system. The workspaces were designed in SolidWorks and printed using ABS (acrylonitrile butadiene styrene) on a Stratasys F370 printer. A commercially available endoscopic capsule device (PillCam™ COLON 2 System, Medtronic) is chosen as the magnetic agent for this study. PillCam™ exhibits soft magnetic properties and can be temporarily magnetized for manipulation inside VORIACS. As such, the PillCam™ used in our experiments was unmodified, with all manipulations relying on the inherent magnetic properties of the capsule. Fig. 1a shows the schematics of a top view of the VORIACS system along with the PillCam™ in a zoomed view of the workspace. The workspace was designed to mimic a portion of the GI tract, including the terminal portion of the small intestine (ileum) and the large intestine with both connecting at the ileocecal valve. For better controllability, the PillCam™ was kept submerged in a viscous medium (pure glycerin) during experiments. The activation of the electromagnets with 9 V or 4.5 A (15% of the maximum available power) was enough for experiments, which helped avoid rapid heating of the VORIACS and activation of any external cooling system.

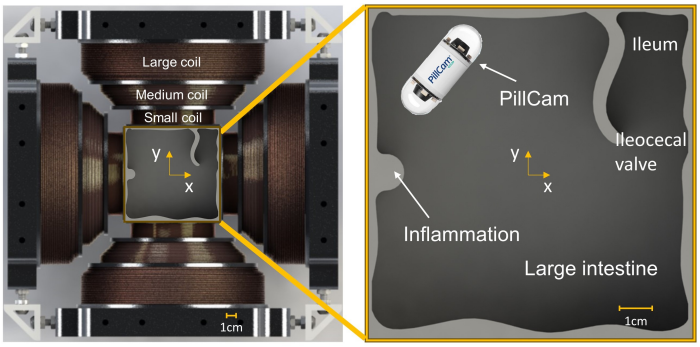


Fig. 1. (a) Schematic showing the VORIACS system, composed of 12 coils surrounding an experimental workspace 10 mm on a side. (b) An enlarged view of the 3D printed workspace and PillCam™ endoscope. Regions of the 3D printed workspace are designed to mimic features of the GI tract (see labels).

2.2. *Camera Calibration and Robot Tracking*

As the camera is not fixed to the coil system, a calibration process is needed prior to system operation. This calibration procedure involves affixing five green labels at the corners and center of the workspace as reference points. While three points are theoretically sufficient for defining the plane of the workspace, we employ five points to min-

imize errors and enhance the accuracy of the plane's representation. A perspective matrix can be computed by analyzing label positions in both the coil system frame and the camera frame. When this matrix is applied to a position vector in the camera frame, the corresponding position vector in the coil system frame can be calculated. This transformation hinges on the interrelation between the two frames and the conversion factor between pixel and millimeter scales.

Precise control of the PillCam™ (robot) requires knowing its accurate position. To accomplish this, a visual tracking method is employed at two symmetrically marked red and blue points on the robot's surface. The midpoint of the line segment connecting these two points is defined as the robot's centroid position, while the orientation of this segment corresponds to the robot's orientation. By monitoring the changes in the position of the red and blue points, we can effectively track the robot's position and orientation.

2.3. *Finite Element Analysis of VORIACS*

The control of the robot relies on the magnetic field distribution data generated from all twelve individual coils in the VORIACS system. This study employs finite element analysis (FEA) based modeling of the electromagnets to generate the magnetic field and gradient data required for control experiments. The FEA simulation was conducted using COMSOL Multiphysics' AC/DC module. Fig. 2 illustrates the FEA results for a small coil and a coil unit of the VORIACS system consisting of concentric small, medium, and large coils.

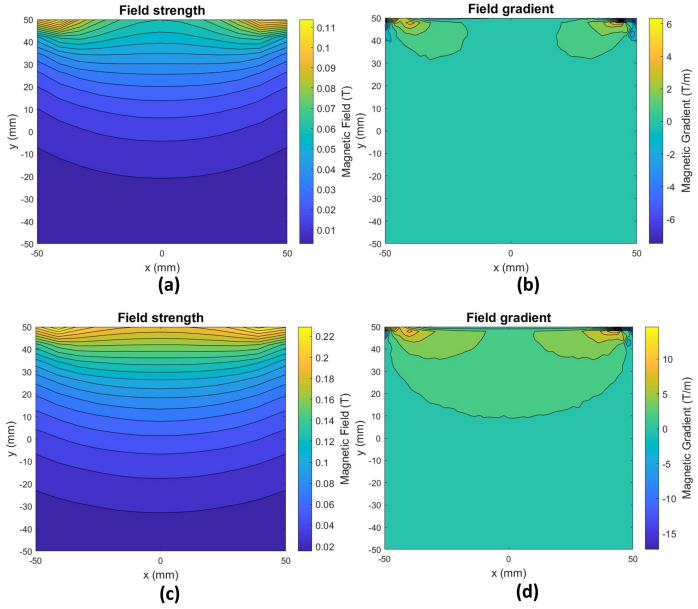


Fig. 2. FEA results showing (a) field strength and (b) field gradient norm distribution along the axis of a small coil, and (c) field strength and (d) field gradient for a coil unit, where the coils are located on the top of the figures and input is 60 V.

The simulation parameters, such as material properties, resistance values, and the number of windings, are configured to mirror the characteristics of the physical system.[20] The simulation domain is a cube centered on the experimental workspace coordinate system.

Since all coil units have identical characteristics, simulation is performed on a single coil unit to produce data sets for the entire VORIACS. These data sets encompass the field strength in both the x- and y-directions, at points uniformly dispersed across a 100×100 mm^2 workspace. The spatial resolution is maintained at a 2 mm interval between adjacent data points. All of these data sets are generated under the condition that the coil is supplied with a maximum power input of 60 V. To validate the accuracy of the FEA data, we measured magnetic fields at 8 mm intervals within the workspace using a Gauss meter and calculated the error between the measured data and the FEA data. The average error (0.52 mT) is negligible compared to the magnitude of the field, demonstrating the reliability of the FEA data.

2.4. *Dynamics of VORIACS*

A magnetic agent has a magnetic moment vector, $\boldsymbol{m}$, characterizing both the magnetic strength and the orientation of the agent. When subjected to a specific magnetic field $\boldsymbol{B}$, the magnetic agent experiences both a magnetic force $\boldsymbol{F}$ and a torque $\boldsymbol{T}$ described by

$$\boldsymbol{F} = (\boldsymbol{m}^T \cdot \nabla)\boldsymbol{B} = \begin{bmatrix} \boldsymbol{m}^T \frac{\partial \boldsymbol{B}}{\partial x} \\ \boldsymbol{m}^T \frac{\partial \boldsymbol{B}}{\partial y} \\ \boldsymbol{m}^T \frac{\partial \boldsymbol{B}}{\partial z} \end{bmatrix}, \tag{1}$$

$$\boldsymbol{T} = \boldsymbol{m} \times \boldsymbol{B}. \tag{2}$$

The strength of magnetic field $\boldsymbol{B_i}$ generated by the ith coil at a particular point is directly proportional to the current I_i, with the orientation of the magnetic field remaining constant. Consequently, the relationship between force, torque, and currents is

$$\begin{bmatrix} F_x \\ F_y \\ F_z \\ \boldsymbol{T} \end{bmatrix} = \begin{bmatrix} \boldsymbol{m}^T \begin{bmatrix} \frac{\partial \widetilde{\boldsymbol{B_1}}}{\partial x} \frac{\partial \widetilde{\boldsymbol{B_2}}}{\partial x} \cdots \frac{\partial \widetilde{\boldsymbol{B_{12}}}}{\partial x} \end{bmatrix} \\ \boldsymbol{m}^T \begin{bmatrix} \frac{\partial \widetilde{\boldsymbol{B_1}}}{\partial y} \frac{\partial \widetilde{\boldsymbol{B_2}}}{\partial y} \cdots \frac{\partial \widetilde{\boldsymbol{B_{12}}}}{\partial y} \end{bmatrix} \\ \boldsymbol{m}^T \begin{bmatrix} \frac{\partial \widetilde{\boldsymbol{B_1}}}{\partial z} \frac{\partial \widetilde{\boldsymbol{B_2}}}{\partial z} \cdots \frac{\partial \widetilde{\boldsymbol{B_{12}}}}{\partial z} \end{bmatrix} \\ \boldsymbol{m} \times \widetilde{\boldsymbol{B}} \end{bmatrix} \begin{bmatrix} I_1(t) \\ I_2(t) \\ \cdots \\ I_{12}(t) \end{bmatrix}, \tag{3}$$

where F_x, F_y, and F_z correspond to forces in the x-, y-, and z-directions, respectively. $\widetilde{\boldsymbol{B_i}}$ represents the magnetic field strength $\boldsymbol{B_i}$ when the current is set to 1 ampere for the ith coil. $\widetilde{\boldsymbol{B}}$ is the sum of all $\widetilde{\boldsymbol{B_i}}$, i.e. $\sum_{i=1}^{12} \widetilde{\boldsymbol{B_i}}$.

Eq. (3) serves as the fundamental dynamics equation for controlling a single magnetic agent with 12 electromagnetic coils. Nonetheless, since the magnetic agent mostly moves in 2D and quickly aligns with the magnetic field,

z-direction motion and dynamic rotational aspects are not needed. Consequently, the simplified equation is

$$\begin{bmatrix} F_x \\ F_y \\ \omega_o \cdot \boldsymbol{B}_x \\ \omega_o \cdot \boldsymbol{B}_y \end{bmatrix} = \begin{bmatrix} \boldsymbol{m}^T \begin{bmatrix} \frac{\partial \widetilde{\boldsymbol{B_1}}}{\partial x} \frac{\partial \widetilde{\boldsymbol{B_2}}}{\partial x} \cdots \frac{\partial \widetilde{\boldsymbol{B_{12}}}}{\partial x} \end{bmatrix} \\ \boldsymbol{m}^T \begin{bmatrix} \frac{\partial \widetilde{\boldsymbol{B_1}}}{\partial y} \frac{\partial \widetilde{\boldsymbol{B_2}}}{\partial y} \cdots \frac{\partial \widetilde{\boldsymbol{B_{12}}}}{\partial y} \end{bmatrix} \\ \widetilde{\boldsymbol{B_1}}_x \widetilde{\boldsymbol{B_2}}_x \cdots \widetilde{\boldsymbol{B_{12}}}_x \\ \widetilde{\boldsymbol{B_1}}_y \widetilde{\boldsymbol{B_2}}_y \cdots \widetilde{\boldsymbol{B_{12}}}_y \end{bmatrix} \begin{bmatrix} I_1(t) \\ I_2(t) \\ \cdots \\ I_{12}(t) \end{bmatrix}. \quad (4)$$

Here $\boldsymbol{m}$ transforms into a 2×1 vector, which symbolizes the magnetic moment of the agent in the x-y plane. F_x and F_y are the desired forces added to the robot. $\boldsymbol{B}_x$ and $\boldsymbol{B}_y$ represent components of a unit vector of the magnetic field at the robot's position. ω_o signifies the coefficient assigned to the orientation component, compensating the difference in scale between field strength and gradient, and to some extent, determining the relative weight of the orientation compared to position in the control process. We re-express Eq. (4) as $\boldsymbol{C} = \boldsymbol{A} \cdot \boldsymbol{I}$ for convenience.

Eq. (4) serves as the simplified dynamics equation for the VORIACS system, establishing a mapping between the input current field and the desired control output field. The matrix $\boldsymbol{A}$ takes on the dimensions of 4×12 and is determined by $\boldsymbol{m}$, $\widetilde{\boldsymbol{B_i}}$, $\partial \widetilde{\boldsymbol{B_i}}/\partial x$, and $\partial \widetilde{\boldsymbol{B_i}}/\partial y$. It can be computed once the robot's position and orientation are determined.

It is crucial to note that when the determinant of $\boldsymbol{A} \cdot \boldsymbol{A}^T$ approaches zero (i.e., $\boldsymbol{A}$ is ill-conditioned), the control system may become highly sensitive or unstable if the input current is directly calculated using $\boldsymbol{A}$. When the robot is positioned at θ orientation, the areas that make matrix $\boldsymbol{A}$ ill-conditioned are defined as the singular regions at θ.

With the matrix $\boldsymbol{A}$ and the desired output vector $\boldsymbol{C}$, the input current vector $\boldsymbol{I}$ can be determined by solving the equation $\boldsymbol{C} = \boldsymbol{A} \cdot \boldsymbol{I}$. This is a linear least-squares problem. Several methods are available to solve such problems, including Pseudo-inverse, QR decomposition, and Upper-Lower decomposition. However, in consideration of stability, robustness, and the quality of solutions, we use the Singular Value Decomposition (SVD) method. If the $\boldsymbol{C}$ is in the range of $\boldsymbol{A}$, SVD will find the solution that has the minimum norm solution. If it is not in the range, then the least-squares solution will be found.[21] SVD is also more stable than other methods when $\boldsymbol{A}$ is not well-conditioned or even rank-deficient. In this study, we have adopted the economic form of SVD, also known as Economy SVD. The SVD of matrix $\boldsymbol{A}$ in its economic form can be presented as

$$\boldsymbol{A} = \boldsymbol{U}\boldsymbol{S}\boldsymbol{V}^T, \quad (5)$$

where $\boldsymbol{A} \in \mathbb{R}^{12 \times 4}$. The SVD yields three key matrices. $\boldsymbol{V}$ is a 4×4 square matrix containing orthonormal eigenvectors derived from the product $\boldsymbol{A}^T \cdot \boldsymbol{A}$. $\boldsymbol{S}$ is a 4×4 diagonal matrix, with its elements being equal to the square root of the positive eigenvalues stemming from either $\boldsymbol{A}^T \cdot \boldsymbol{A}$ or $\boldsymbol{A} \cdot \boldsymbol{A}^T$, as both of them share the same set of positive eigenvalues. Notably, in contrast to the complete form of SVD, the economic form's $\boldsymbol{S}$ matrix is reduced to 4×4, omitting any additional rows of zeros. $\boldsymbol{U}$ is a 12×4 matrix and is constructed from a 12×12 square matrix containing orthonormal eigenvectors of $\boldsymbol{A} \cdot \boldsymbol{A}^T$, by removing the corresponding columns that would multiply with those excluded zeros in $\boldsymbol{S}$. The current vector $\boldsymbol{I}$ can be computed as

$$\boldsymbol{I} = \boldsymbol{V} \cdot (\boldsymbol{S}^{-1}) \cdot \boldsymbol{U}^T \cdot \boldsymbol{A}. \quad (6)$$

If the maximum current exceeds 30 A, all current values will be reduced proportionally to ensure they remain within the system's limits.

2.5. *Controller for Singularity*

Despite the stability advantage that SVD offers over other methods in solving linear least squares problems, control systems can encounter challenges when matrix $\boldsymbol{A}$ is ill-conditioned or even rank-deficient. Based on comprehensive testing conducted on our system, the most prevalent cause for undesirable control results is that $\boldsymbol{A}$ conforms to the following equation:

$$\Sigma(k_n \cdot \boldsymbol{C}_n) = k_i \cdot \boldsymbol{C}_i + \boldsymbol{\epsilon}. \quad (7)$$

Eq. (7) signifies that some columns $\boldsymbol{C}$ of $\boldsymbol{A}$ are close to linear dependence. As a result, huge variations in currents I_n and I_i only yield minor changes in $\boldsymbol{\epsilon}$ in the control output. Consequently, a solution involving a significantly large change in current is calculated by Eq. (4), subsequently causing randomness in robot motion. Moreover, when $\boldsymbol{C}$ is not in the range of $\boldsymbol{A}$, the desired current will be very large to minimize the residual error. Then, the huge currents are reduced proportionally to adhere to the system's limitations. This adjustment can lead to one of the two outcomes: either the translation force becomes insufficient to overcome the drag force exerted by glycerin, or the magnetic field's strength is insufficient to maintain the robot in its desired orientation.

Various techniques have been developed to enable manipulators to move through singularity by breaking the linear dependent constraints, thereby making the Jacobian matrix non-singular.[22] Although VORIACS is a magnetic actuation system, a similar approach can be employed to address singularity issues by eliminating one of the linear dependent columns, thereby disrupting Eq. (7). This forms the foundational concept behind the controller for singularity. The process entails generating 12 matrices, $\boldsymbol{B_i}$, by removing one column from $\boldsymbol{A}$ in sequence. Subsequently, the condition number of $\boldsymbol{B_i}$ is computed for each matrix, and the one with the smallest value, indicative of being relatively more well-conditioned, is selected. The controller then proceeds to employ these 11 coils to control the robot's motion. The current corresponding to the removed column is set to 0.

This controller is engaged when the absolute value of the determinant of $\boldsymbol{A} \cdot \boldsymbol{A}^T$ falls below a predefined threshold, signifying that $\boldsymbol{A}$ is ill-conditioned.

2.6. *Closed-Loop Control*

If a robot is instructed to move towards a user-specified position (x_{tar}, y_{tar}), the error $\boldsymbol{e}$ can be defined as

$$\boldsymbol{e} = \begin{bmatrix} x_{tar} - x_{rob} \\ y_{tar} - y_{rob} \end{bmatrix}, \tag{8}$$

where (x_{rob}, y_{rob}) is the current position of the robot.

A conventional proportional-integral-derivative (PID) controller is employed for closed-loop control, utilizing the error $\boldsymbol{e}$. The desired force to be applied to the robot is expressed as

$$\begin{bmatrix} F_x \\ F_y \end{bmatrix} = k_p \cdot \boldsymbol{e} + k_i \cdot \int \boldsymbol{e} dt + k_d \cdot \dot{\boldsymbol{e}}, \tag{9}$$

where k_p, k_i, and k_d are 5, 0.1, and 1, respectively. The orientation component is not included in the error $\boldsymbol{e}$ as the robot can easily align with the magnetic field direction unless the field strength is too low. The desired unit field can be represented as

$$\begin{bmatrix} B_x \\ B_y \end{bmatrix} = \begin{bmatrix} sin(\theta_{tar}) \\ cos(\theta_{tar}) \end{bmatrix}, \|\boldsymbol{B}\| = 1, \tag{10}$$

where θ_{tar} is the target orientation in the coil system frame.

2.7. *Constraint on Current's Changing Rate*

The imposition of a constraint on the rate of change in current serves two primary purposes. First, it addresses the sensitivity of the derivative component in the PID controller. Due to the short control loop time, even relatively minor positional errors can result in significant velocity errors, potentially influencing the controller's stability. By introducing the constraint, the controller's output becomes more stable when confronted with sudden changes in input. Secondly, electromagnetic coils inherently possess inductance, which imposes a physical limitation on the maximum rate of current change. This constraint ensures that the desired rate stays within physical limits, guaranteeing that the desired current values are effectively input into the system. This constraint also serves as a protective measure for the electrical components of the system.

Instead of imposing a static limit on the current's changing rate, an optimal control approach is integrated into Eq. (4) as a dynamic restriction and is presented by

$$\begin{bmatrix} F_x \\ F_y \\ \omega_o B_x \\ \omega_o B_y \\ \omega_c I_1(t-1) \\ \omega_c I_2(t-1) \\ \dots \\ \omega_c I_{12}(t-1) \end{bmatrix}_{16\times 1} = \begin{bmatrix} \boldsymbol{A}_{4\times 12} \\ \omega_c \widetilde{\boldsymbol{I}}_{12\times 12} \end{bmatrix}_{16\times 12} \begin{bmatrix} I_1(t) \\ I_2(t) \\ \dots \\ I_{12}(t) \end{bmatrix}_{12\times 1} \tag{11}$$

where $\widetilde{\boldsymbol{I}}_{12\times 12}$ is a 12×12 identity matrix and $\omega_c \in \mathbb{R}$.

The first four rows of Eq. (11) remain identical to Eq. (4), while the rest rows synchronize new currents with the currents from the last control loop. The variable ω_c represents the weight applied to these rows, with a larger ω_c indicating a more substantial constraint on the rate of current change. Irrespective of the chosen value of ω_c, the system ensures that the output currents reach the desired levels without any steady-state error as long as they remain constant.

3. Results

3.1. *Singularity Comparison*

Given that there are three coils constituting a coil unit on one side, the control of the robot can be executed using either a single coil or the entire coil unit. To find out the difference between coil units and single coils in control, a comparative analysis of the singular regions in 4-coil system and 12-coil system control is performed and shown in Fig. 3.

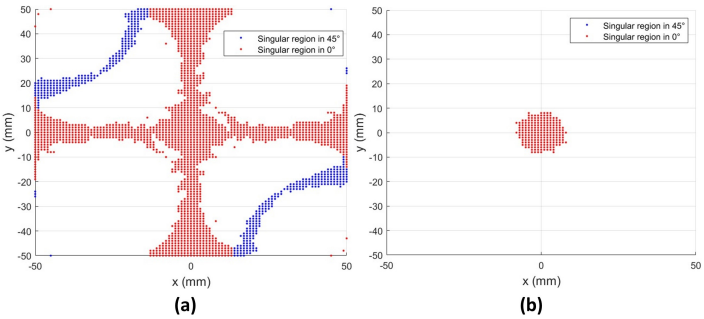


Fig. 3. Singular region comparison between the 4-coil system and 12-coil system control. The singular regions in (a) 4-coil system control and (b) 12-coil system control for field orientations at 0 and 45 degrees.

A specific point is deemed singular at a given orientation if the 2-norm condition number of the control matrix is below 200.[20] It is crucial to emphasize that points not visualized in the figure may still be in proximity to the threshold, indicating that while they may not exhibit severe singularity problems, the control could still be affected to some extent. Here, we choose the 0-degree and 45-degree orientations of the magnetic field for singularity analysis. As in Fig. 3a, the singular region across the workspace is significantly smaller at 45 degrees than 0 degrees with 4-coil system control. Notably, with 12-coil system control, the singularity problem is mitigated in most regions, with only the center area retaining singularity concern at 0 degrees (Fig. 3b). In the following sections, we will explore different control approaches to solving singularity issues as well as the robot's performance in following different trajectories at these orientations.

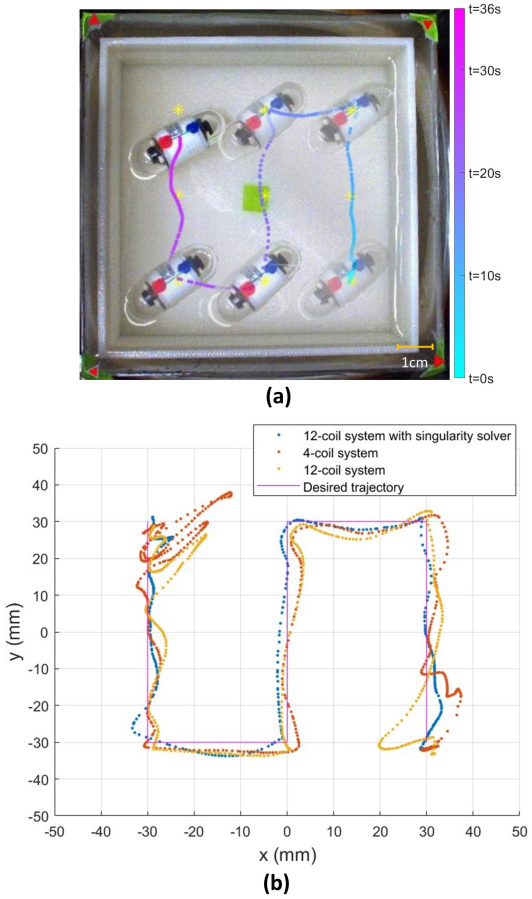


Fig. 4. (a) PillCam™ at different time points tracking the S-shaped trajectory at 45-degree orientation for the 12-coil system with singularity solver. (b) Comparative trajectories for the three control methods along with the desired trajectory at the 45-degree orientation.

Table 1. Errors for trajectory tracking at 45 degrees. E_p and E_o are the RMS position and orientation errors, respectively.

Method	E_p (mm)	E_o (°)
12-coil system with singularity solver	1.51	8.0
12-coil system	2.77	10.8
4-coil system	2.80	13.7

3.2. *Trajectory Tracking Performance with Different Control Methods*

In this study, S-shaped trajectories spanning the entire workspace for the magnetic field orientation at 0 and 45 degrees are utilized to evaluate the performance of different control methods. Three distinct control methods are employed: 4-coil system, 12-coil system (see Section 2.4), and 12-coil system with singularity solver (see Section 2.5). The size of the trajectory at 0 degrees is chosen to be smaller than the trajectory at 45 degrees to prevent collisions between the PillCam™ and the boundary walls during navigation across the workspace.

3.2.1. *Trajectory tracking at 45-degree orientation*

The PillCam™ is tasked with traversing the S-shaped trajectory while maintaining a 45-degree orientation in the coil system coordinates. Three tests were conducted for each of the three control methods along this trajectory. Fig. 4a shows the trajectory and the PillCam™ at different time points for the 12-coil system with singularity solver.

PillCam™'s trajectories for the three control methods in comparison to the desired trajectory are depicted in Fig. 4b, and their associated root mean square (RMS) errors from the desired trajectory and orientation are reported in Table 1. The trajectories of all three methods exhibit more errors in the up-left and down-right corners, aligning with the singular region illustrated in Fig. 3. Notably, the 12-coil system with a singularity solver demonstrates both the smallest RMS position and orientation errors among the three methods. This outcome is reasonable as a significant portion of errors arises from the singular region. The 12-coil system inherently possesses a much smaller singular region compared to the 4-coil system, and the singularity solver further effectively mitigates the problems.

3.2.2. *Trajectory tracking at 0-degree orientation*

Next, the PillCam™ is controlled to follow an S-shaped trajectory at 0-degree orientation using the three control methods. Fig. 5a illustrates the experimental trajectory and the PillCam™ at different time points for the 12-coil system with singularity solver, while Fig. 5b shows the comparative trajectories for the three control methods along with the desired S-shaped trajectory at 0 degrees.

As the robot is expected to encounter singularities along the x- and y-axes (see Fig. 3), experimental trajectories at 0 degrees for all three control methods show increased deviations from the desired trajectory when approaching or departing from the x- and y-axes (see Fig. 5). Additionally, certain trajectories display overshooting, wherein the robot receives excessive force in the singular region, leading to upsurged velocities. The RMS position and orientation tracking errors for the three control methods are reported in Table 2. Here again, the 12-coil system with singularity solver has the lowest RMS position and orientation tracking errors among all. However, the RMS errors at 0 degrees are greater than the errors at 45 degrees (compare Table 2 with Table 1).

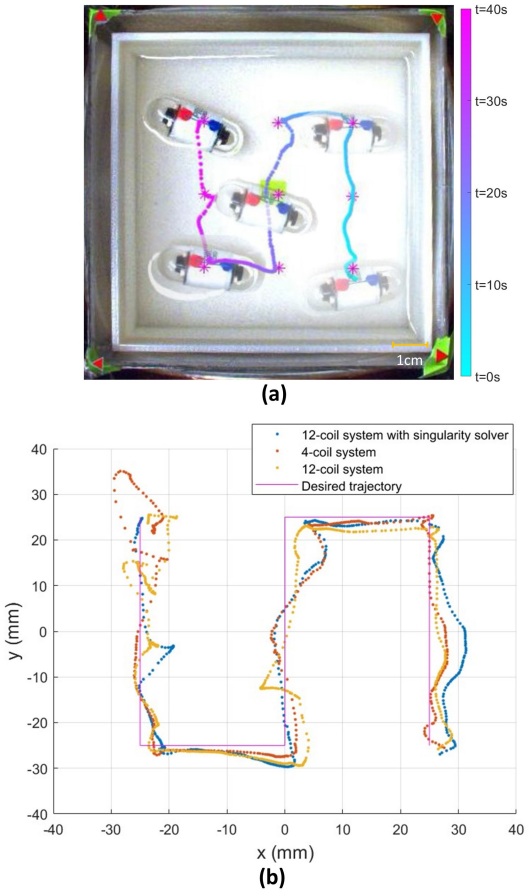


Fig. 5. (a) PillCam™ at different time points tracking the S-shaped trajectory at 0-degree orientation for the 12-coil system with singularity solver. (b) Comparative trajectories for the three control methods along with the desired trajectory at the 0-degree orientation.

Table 2. Errors for trajectory tracking at 0 degrees. E_p and E_o are the RMS position and orientation errors, respectively.

Method	E_p (mm)	E_o (°)
12-coil system with singularity solver	2.11	10.8
12-coil system	3.71	17.7
4-coil system	4.20	18.3

The comparative trajectory tracking experiments conducted for the 45-degree and 0-degree orientations highlight the superior performance of the 12-coil system with singularity solver, outperforming the other two methods. Conversely, the 4-coil system has relatively poorer results among the three tested methods. Even though all the trajectories include singular regions, the 12-coil system with singularity solver effectively mitigates the associated issues. Given that the PillCam™ is a soft magnet, the RMS position tracking error for this control method is about 6.44% of the PillCam™'s body length, which is a favorable outcome.

3.3. *Potential Medical Application*

This experiment aims to demonstrate a potential medical application for Crohn's disease using the PillCam™. Although PillCam™ is a passive endoscopic device, with the integration of a magnetic actuation system, it can be effectively controlled to focus on specific targets with precision.

In the course of the experiment demonstrated in Fig. 6, the PillCam™ initiates in the segment corresponding to the distal ileum, traverses the ileocecal valve, and enters the large intestine. Subsequently, it executes a rotational movement at the same position to comprehensively scan the surrounding area and identify the inflammation tissue. Following this, the PillCam™ performs a curved scan of that tissue towards the identified tissue and approaches it for another scan. The experiment was performed using the 12-coil system with a singularity solver, as it has demonstrated superior performance in previous experiments.

Three tests were conducted, yielding an RMS position error of 1.72 mm (5.25% of PillCam™'s body length) and an RMS orientation error of 8.5°. Fig. 7 depicts the trajectory and corresponding errors. The tracking error is computed and reported for manipulation of the PillCam™ outside the ileocecal valve. The observed peak in position error between 21 s and 26 s is the overshooting caused by a long-distance acceleration before the first curve scan.



Fig. 6. Closed-loop controlled manipulation of the PillCam™ for possible inspection of inflammation or other relevant tissue conditions in the GI tract. PillCam™ is first manipulated in proximity to the anomaly, then makes a sweep around the anomaly at a constant radial distance of ∼35 mm, and finally moves closer to make a second pass imaging the anomaly at a constant radial distance of ∼20 mm.

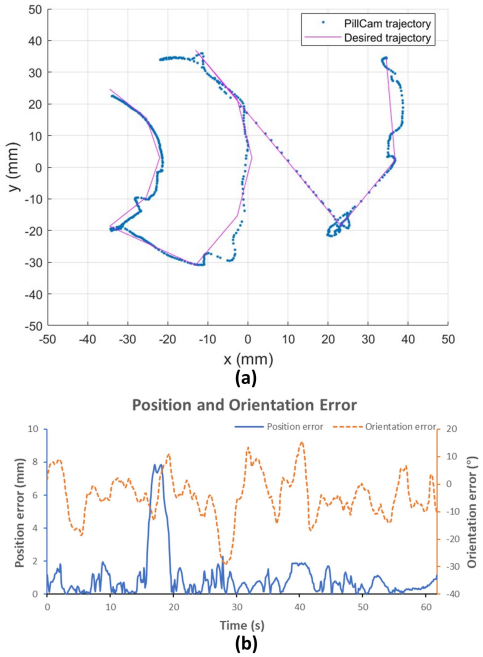


Fig. 7. (a) PillCam™'s trajectory in comparison to the desired trajectory in the demonstration of medical application. (b) Position and orientation error plots in trajectory tracking for medical application of PillCam™.

4. Discussion and Conclusion

Despite the achievements, there are limitations to this work. The model treats the PillCam™ as a permanent magnet, overlooking distinctions between soft and hard magnets. The fluid drag force exerted on PillCam™, which is potentially significant at high velocities, is not considered. These two limitations are primary sources of errors in the experiments. Additionally, the scope of the method is confined to 2D motion.

Future work in this domain could involve the development of a more precise model for PillCam™, enhancing control accuracy. Furthermore, exploring the usage of coils along the z-axis could extend the scope of the method to include tests in 3D, providing a more comprehensive application of the system.

This paper reports a closed-loop control method using a novel nested 12-coil electromagnetic system along with finite element analysis-based magnetic field data, a PID controller, and a singularity solver. The experiments conducted demonstrate the effectiveness of the proposed control method in mitigating singularity problems and achieving high-precision control of a PillCam™ capsule endoscope. As a clinically relevant tool for assessing Crohn's disease,[23] improved Pillcam™ manipulation capabilities may provide access to advanced diagnostic imaging data for physicians. Here, a conceptual experiment illustrates the potential application of employing a magnetic actuation system to aid PillCam™ in detecting Crohn's disease.

Acknowledgments

We thank Jakub Piwowarczyk for helping us with the VORIACS system setup and Adam May for sharing useful insights on the application demonstration. This research has been generously funded by the National Science Foundation's Foundational Research in Robotics CAREER program under award number 2144348. The views and opinions expressed in this work are solely those of the authors and do not necessarily reflect the official stance of the National Science Foundation.

References

[1] M. Sitti, H. Ceylan, W. Hu, J. Giltinan, M. Turan, S. Yim and E. Diller, Biomedical applications of untethered mobile milli/microrobots, *Proc. IEEE* **103**(2) (2015) 205–224.

[2] B. J. Nelson, I. K. Kaliakatsos and J. J. Abbott, Microrobots for minimally invasive medicine, *Annu. Rev. Biomed. Eng.* **12** (2010) 55–85.

[3] J. J. Abbott, E. Diller and A. J. Petruska, Magnetic methods in robotics, *Annu. Rev. Control Rob. Auton. Syst.* **3** (2020) 57–90.

[4] S. Yim and M. Sitti, Design and rolling locomotion of a magnetically actuated soft capsule endoscope, *IEEE Trans. Rob.* **28**(1) (2011) 183–194.

[5] D. Ye, J. Xue, S. Yuan, F. Zhang, S. Song, J. Wang and M. Q.-H. Meng, Design and control of a magnetically-actuated capsule robot with biopsy function, *IEEE Trans. Biomed. Eng.* **69**(9) (2022) 2905–2915.

[6] L. O. Mair, X. Liu, B. Dandamudi, K. Jain, S. Chowdhury, J. Weed, Y. Diaz-Mercado, I. N. Weinberg and A. Krieger, Magnetosuture: Tetherless manipulation of suture needles, *IEEE Trans. Med. Rob. Bionics* **2**(2) (2020) 206–215.

[7] O. Erin, X. Liu, J. Ge, J. Opfermann, Y. Barnoy, L. O. Mair, J. U. Kang, W. Gensheimer, I. N. Weinberg, Y. Diaz-Mercado *et al.*, Overcoming the force limitations of magnetic robotic surgery: Magnetic pulse actuated collisions for tissue-penetrating-needle for tetherless interventions, *Adv. Intell. Syst.* **4**(6) (2022) p. 2200072.

[8] W. Pryor, Y. Barnoy, S. Raval, X. Liu, L. Mair, D. Lerner, O. Erin, G. D. Hager, Y. Diaz-Mercado and A. Krieger, Localization and control of magnetic suture needles in cluttered surgical site with blood and tissue, *2021 IEEE/RSJ International Conference on Intelligent Robots and Systems (IROS)*, (2021), pp. 524–531.

[9] Y.-L. Liu, D. Chen, P. Shang and D.-C. Yin, A review of magnet systems for targeted drug delivery, *J. Controlled Release* **302** (2019) 90–104.

[10] W. Chen, J. Sui and C. Wang, Magnetically actuated capsule robots: A review, *IEEE Access* **10** (2022) 88398–88420.

[11] R. A. Enns, L. Hookey, D. Armstrong, C. N. Bernstein, S. J. Heitman, C. Teshima, G. I. Leontiadis, F. Tse and D. Sadowski, Clinical practice guidelines for the use of video capsule endoscopy, *Gastroenterology* **152**(3) (2017) 497–514.

[12] L. J. Sliker, G. Ciuti, M. E. Rentschler and A. Menciassi, Frictional resistance model for tissue-capsule endoscope sliding contact in the gastrointestinal tract, *Tribol. Int.* **102** (2016) 472–484.

[13] A. J. Petruska, J. Edelmann and B. J. Nelson, Model-based calibration for magnetic manipulation, *IEEE Trans. Magn.* **53**(7) (2017) 1–6.

[14] O. Erin, S. Raval, T. J. Schwehr, W. Pryor, Y. Barnoy, A. Bell, X. Liu, L. O. Mair, I. N. Weinberg, A. Krieger *et al.*, Enhanced accuracy in magnetic actuation: Closed-loop control of a magnetic agent with low-error numerical magnetic model estimation, *IEEE Rob. Autom. Lett.* **7**(4) (2022) 9429–9436.

[15] S. Raval, O. Erin, X. Liu, L. O. Mair, W. Pryor, Y. Barnoy, I. N. Weinberg, A. Krieger and Y. Diaz-Mercado, Magnetic model calibration for tetherless surgical needle manipulation using zernike polynomial fitting, *2021 IEEE 21st International Conference on Bioinformatics and Bioengineering (BIBE)*, (2021), pp. 1–6.

[16] A. J. Petruska and B. J. Nelson, Minimum bounds on the number of electromagnets required for remote magnetic manipulation, *IEEE Trans. Rob.* **31**(3) (2015) 714–722.

[17] A. N. Tikhonov, A. Goncharsky, V. V. Stepanov, A. G. Yagola, A. Tikhonov, A. Goncharsky, V. Stepanov and A. Yagola, *Numerical methods for the approximate solution of ill-posed problems on compact sets* (Springer, 1995).

[18] H. Zhao, J. Leclerc, M. Feucht, O. Bailey and A. T. Becker, 3d path-following using mrac on a millimeter-scale spiral-type magnetic robot, *IEEE Rob. Autom. Lett.* **5**(2) (2020) 1564–1571.

[19] K. T. Nguyen, M. C. Hoang, G. Go, B. Kang, E. Choi, J.-O. Park and C.-S. Kim, Regularization-based independent control of an external electromagnetic actuator to avoid singularity in the spatial manipulation of a microrobot, *Control Eng. Pract.* **97** (2020) p. 104340.

[20] O. Erin, X. Chen, A. Bell, S. Raval, T. Schwehr, X. Liu, P. Addepalli, L. O. Mair, I. N. Weinberg, Y. Diaz-Mercado and A. Krieger, Ultra-strong magnetic actuation: Optimized variable outer radius individually addressable coil stacks (voriacs) generates large magnetic forces, *Sci. Rep.* (Under Review).

[21] J. W. Demmel, 3. linear least squares problems, *Applied Numerical Linear Algebra*, (SIAM, 1997), pp. 105–133.

[22] D. Oetomo and M. H. Ang Jr, Singularity robust algorithm in serial manipulators, *Rob. Comput. Integr. Manuf.* **25**(1) (2009) 122–134.

[23] L. Goran, A. M. Negreanu, A. Stemate and L. Negreanu, Capsule endoscopy: Current status and role in crohn's disease, *World J. Gastrointest Endosc.* **10**(9) (2018) p. 184.